Effect of part thickness on the microstructure and tensile properties of 316L parts produced by laser powder bed fusion

Advances in Industrial and Manufacturing Engineering 2 (2021) 100037

Contents lists available at ScienceDirect

Advances in Industrial and Manufacturing Engineering

journal homepage: www.journals.elsevier.com/advances-in-industrial-and-manufacturing-engineering

Effect of part thickness on the microstructure and tensile properties of 316L parts produced by laser powder bed fusion

Alexander Leicht, Camille Pauzon *, Masoud Rashidi, Uta Klement, Lars Nyborg, Eduard Hryha

Chalmers University of Technology, Department of Industrial and Material Science, Rännvägen 2A, SE-412 96, Göteborg, Sweden

ARTICLE INFO

Keywords:
Stainless steel
Laser powder bed fusion
Design for additive manufacturing
Mechanical properties
Microstructure
Build geometry

ABSTRACT

Additive manufacturing provides a unique possibility to manufacture parts with advanced design and thin-walled structures. To explore thin-wall capacity, laser powder bed fusion was employed to fabricate 316 L samples with different section thicknesses. A detailed microstructure characterization was then carried out, and tensile properties were assessed. It was found that reducing the part thickness did not affect the microstructure but did reduce the tensile properties. Samples with 1 mm thickness exhibited the lowest yield strength of 457 ± 11 MPa and elongation to fracture of 49 ± 20%, while the tensile properties improved when the sample thickness was increased to 3 mm. The 3 mm thick samples generated tensile properties comparable to those of standard dimensions. The results emphasize that part thickness must be considered when assessing mechanical properties and must be adjusted when performing design optimization and simulations of samples produced with laser powder bed fusion.

1. Introduction

Additive manufacturing (AM) confers many advantages, including increased production flexibility, product customization, reduced waste of resources, and reduced lead times (Thomas, 2016; Sames et al., 2016; Berman, 2012). The most common AM process for fabricating metal parts is laser-based powder bed fusion (L-PBF) (DebRoy et al., 2018). This process offers a unique possibility to manufacture advanced product designs and a novel way to create lightweight products like lattice structures owing to its capabilities of allowing a high degree of freedom in product design.

Stainless steel of type 316 L has been recognized as an important engineering material in a wide range of applications because of its adequate strength and high corrosion resistance. The microstructure of the L-PBF-processed materials consists of large, elongated grains that span over several melt pool boundaries. A fine cellular structure forms inside the crystallographic grains (Wang et al., 2018a, 2018b; Zhong et al., 2016). The cellular structure is associated with the segregation of alloying elements such as Mo at cell boundaries and dislocation networks (Zhong et al., 2016; Wang et al., 2018b). This unique microstructure presents enhanced mechanical properties compared to parts produced using conventional methods (Wang et al., 2018b), and as a result, the ability to manufacture a fully dense part with excellent mechanical properties represents the current state of the art. Such parts are already realized through available hardware and process parameters supplied by numerous technology providers. Kurzynowski et al. (2018) highlighted that the preferential orientation of 316 L stainless steel produced by L-PBF is strongly impacted by laser power and the employed scanning strategy, using a SLM Realizer II 250. Liverani et al. (2017) obtained on a SISMA MYSINT100 system that laser power was the parameter with the strongest influence on the obtained density and strength compared to hatch distance and building orientation for 316 L stainless steel. Finally, Li et al. (2018) showed that laser power, well-established as a major parameter to achieve full density, does not have a significant influence on tribological properties of 316 L stainless steel obtained by L-PBF using a Renishaw AM400 machine.

It is clear based on the available research, that there is a need for further knowledge regarding the effect of sample geometries on the mechanical performance of AM-produced samples. Extensive research has been conducted on the mechanical behavior of lattice structures fabricated using L-PBF. However, most of these studies have focused on the mechanical response of the whole lattice systems, consisting of several topologically ordered unit cells of different designs. Indeed, the strength of the lattice is strongly associated with the geometrical design; the load capacity can also be limited by the mechanical properties of a single strut. It is therefore crucial to understand the effect that reducing

* Corresponding author.
E-mail address: pauzon@chalmers.se (C. Pauzon).

https://doi.org/10.1016/j.aime.2021.100037
Received 26 November 2020; Received in revised form 29 January 2021; Accepted 21 February 2021

the part cross-section has on mechanical performance. Several studies have investigated the generic effect of sample size on mechanical performance for conventional materials of different kinds. For example, for micro-shaped Cu, Yang and Lu (2013) showed that tensile strength, ductility, and work hardening decrease if the ratio of specimen thickness to average grain size is below a specific critical value. The authors explained their findings by referring to the competition between dislocation activities in grains in the center of the part compared to the grains at the part surface.

Furthermore, Kohyama et al. demonstrated the sample size effect on yield strength in the case of 316 L sheets (Kohyama et al., 1991). They verified that below a certain critical thickness, the yield strength decreased, and they pointed out that the relation between the sample thickness and average grain size is a controlling factor. Namely, the yield strength was reduced when the thickness-to-grain-size ratio became less than six. Raulea et al. (2001) found that for pure aluminum sheets, the critical thickness was well above the thickness-to-grain-size ratio of 20. Strnadel et al. (Strnadel and Brumek, 2013) emphasized the role of critical thickness further while also pointing out that the number of grains in relation to the sample thickness changes the deformation mechanism, which could influence the yield point. All the mentioned materials have a face-centered cubic structure. It is therefore likely that AM-fabricated 316 L parts also exhibit a size effect. However, only limited studies have examined the size effect on AM-produced materials.

Furthermore, AM processing will induce differences in surface and bulk microstructure. Part design may alter heat dissipation and thermal condition, the solidification structure, and hence the resulting microstructure. Leicht et al. (2018), for example, analyzed grain morphology and revealed that fine, randomly oriented grain structure was created close to the surface of L-PBF-produced 316 L parts. Niendorf et al. (2014) investigated the texture of cylindrical bars produced with different diameters (5.0–0.65 mm) and demonstrated that the texture changed from random to <001> preferential orientation with reduced diameter. Wang et al. (2018a) showed a similar effect when reducing strut thicknesses (5.0–0.25 mm). They also presented a change in tensile properties but did not consider the generic geometrical impact.

This study aims to explore the role of part thickness in determining design capabilities when utilizing L-PBF. To achieve this, 316 L samples of varying thicknesses were fabricated and evaluated, and their properties were compared with those of standard-dimensioned tensile test samples. Another aim of the study is to provide evidence that sample thickness must be considered when obtaining mechanical data for L-PBF-processed material. To this end, results of the mechanical testing were combined with dedicated microstructure analysis utilizing optical and electron microscopy and including assessment of grain characteristics using electron backscatter diffraction. The results are intended to provide further evidence of the vital role of part design, as illustrated by the function of sample thickness and the possible existence of a critical thickness.

2. Materials and methods

Gas atomized 316 L stainless steel powder with a particle size range of 20–53 μm was provided by Höganäs AB as feedstock material. An EOS M290 (EOS GmbH) machine was used to build the samples. This system has a maximum nominal power of 400 W generated by a Yb-fiber laser with a focus diameter of about 100 μm. The builds were carried out under argon atmosphere with a residual oxygen content below 0.1% and consisted of tensile test samples fabricated vertically along the build direction. The samples were produced with a layer thickness of 20 μm utilizing standard process parameters (under the license *316L_SurfaceM291* version 1.10) designed to provide full density. These parameters have been extensively optimized by the machine manufacturer and consist in a sophisticated sequence of in-fill and contour scannings for the area to be scanned and its edges, respectively, as well as up- and down-skin exposures for the downward and upward facing surfaces, respectively. In addition, a stripe exposure pattern is followed, which is rotated by 67° between layers. *Skywriting* is also applied and is a rather well-established technique on modern systems that compensate energy input variations induced by the acceleration and deceleration of galvano mirrors along a scan vector (Senthilkumaran et al., 2009). This is thus solved by having the laser power off during this acceleration and deceleration lengths.

The tensile samples were made with two different nominal thicknesses, i.e. 1 mm and 3 mm, while the nominal width was fixed at 2.5 mm. The nominal measures of the samples are presented in Fig. 1a. Supplementary samples were also fabricated with dimensions according to ASTM E8/E8M-15a (termed standard bar), as shown in Fig. 1b. No machining was applied to the samples, except for their removal from the build plate. The cross-sections for metallographic examination were prepared from the center of the tensile test bars (red area in Fig. 1a and b). The microstructure was evaluated from the ZX-plane, as shown in Fig. 1c. The samples were mounted and ground down about 1 mm for thinner samples and 2 mm for the standard bar before a final polish to ensure that enough of the surface was removed and that the characterization was conducted in the core. All samples were prepared following Struers recommendations for metallographic preparation; namely, they were ground using sandpaper with a load of 25 N and polished using a 0.25 μm colloidal silica suspension for 10 min. All samples were analyzed and tested in the as-built condition.

Electro-chemical etching in oxalic acid (10 wt%) at 3 V was performed on the polished cross-sections to reveal the microstructures. The densities of the produced samples were determined by image analysis of light optical images using the software ImageJ. Over 25 images from several cross-sections and locations were obtained from each sample at a magnification of 50x. Each image corresponds to an area of roughly 0.8 by 0.8 mm. Results show that all parts had a porosity under 0.03% ± 0.01% regardless of part thickness. The pores were randomly distributed and did not accumulate close to the surface. A scanning electron microscope (Leo Gemini 1550 SEM) equipped with a field-emission gun was used for high-resolution microstructure characterization. Grain orientations and textures were determined by the electron backscattered diffraction (EBSD) technique using a Nordlys II detector (Oxford Instruments) and HKL Channel 5 data processing software. All measurements were performed with a step size of 1.5 μm and an acceleration voltage of 20 kV. All acquired orientation maps were processed after the acquisition, i.e. wild spikes were removed and minor noise reduction (7 nearest neighbors required) was applied. High angle grain boundaries were defined by a misorientation larger than 10° and are illustrated by black lines in the presented orientation maps.

X-ray diffraction (XRD) was employed to determine the phase distribution within the produced samples using a Bruker AXS D8 Advance instrument within the 2θ range between 30° and 140°. The Cr Kα radiation was used, with an acceleration voltage of 35 kV and a current of 40 mA. The PDF- Card 00-033-0397 was used for to identify the recorded peaks.

Tensile testing was conducted at room temperature using an Instron 5500 R machine at a cross-head velocity of 0.025%/s. The strain was obtained by using an extensometer with a maximum span of 10 mm (approximately 35% elongation). The maximum distance of the extensometer was reached since the samples exhibited elongation beyond 35%. The test was therefore paused at 35%, and then continued until fracture with load control. The reported yield strength (0.2% proof stress), ultimate tensile strength, and elongation to fracture represent the average of three individual samples. The elongation to fracture was determined by measuring the gauge length before and after testing, following the ASTM E8/E8M-15a procedure. The thickness of the bars was measured using two different methods. The first method consisted of measuring the thickness and width with a caliper, which represents the standard procedure to assess sample dimensions when performing tensile testing. The second method was to measure the thickness of the sample cross-sections with light optical microscopy. The cross-section measures were obtained by excluding the surface roughness zone to only include

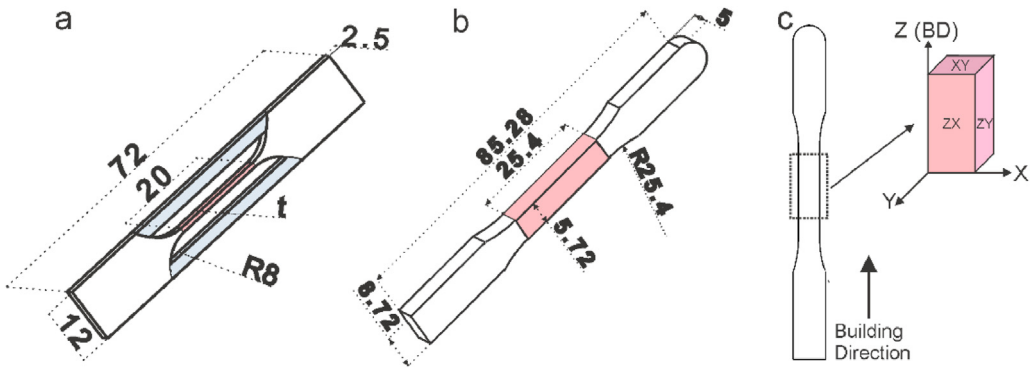

Fig. 1. Schematic drawing of (a) the tensile test bar with thickness **t** indicating the varying thickness (1.0 mm and 3.0 mm) and (b) the standard bar according to ASTM E8/E8M-15a. The grey part shows the support structure. (c) The orientation of the bar and the different cross-sections with respect to the building direction (BD).

bulk material. This method assumes that the thickness and width are the same for all samples of the same nominal dimensions as they must be cut and mounted. As seen in Fig. 2a, both methods result in thicknesses that are greater than the nominal thickness from the CAD design. This difference was observed regardless of thickness and originates from the elliptical-shaped melt pool and the subsequent contour scanning, which is schematically illustrated in Fig. 2b. It can be specified that the linear energy input of the applied contour scanning is slightly reduced compared to that of the in-fill parameters. Furthermore, as can be seen from Fig. 2a, using the standard method (caliper) generates a thickness measure that is 0.16 mm larger than the nominal value, as both surface roughness and the addition from the contour scanning are included in the measure. The light optical microscope method, in contrast, adds approximately 0.04 mm to the nominal measure. The light optical microscope approach is believed to provide the best representation of the amount of load-bearing material. The cross-sectional areas used were 2.64 mm^2, 7.72 mm^2, and 29.03 mm^2.

3. Results

3.1. Microstructure

Fig. 3 shows the microstructure obtained from the standard bar. As can be seen from the lower-magnification image (Fig. 3a), the microstructure is characterized by the presence of melt pool boundaries observed as half-circles. The laser scan direction is rotated after each applied powder layer and therefore appears with different orientations. The black arrows in Fig. 3 indicates a horizontal boundary, meaning that the scan direction was parallel to the investigated cross-section. The half-circles in Fig. 3a (white arrow) are formed when the scan direction is more perpendicular to the observed cross-section. Fig. 3b presents a higher-magnification image showing the fine cellular structure, which develops as a result of the significantly high cooling rate and micro-segregation associated with the process (Wang et al., 2016, 2018b; Saeidi et al., 2015). Indeed, segregation of elements, such as Cr and Mo, occurs along the walls of the cellular structure (Prashanth and Eckert, 2017) and low angle grain boundaries (Wang et al., 2018b). The cells grow along the local maximum temperature gradient (Wang et al., 2016), which can deviate from the macroscopic temperature gradient. In Fig. 3b, numerous cell orientations that pass across melt pool boundaries can be observed. Hence, there is a chance that the actual solidification structure will grow into the next melt pool.

In addition, XRD investigation of the produced 316 L stainless steel of the standard bar and of the thin tensile specimens confirmed the presence of only austenitic phase regardless of the sample design, see Fig. 4. Indeed, it appears that only austenite peaks are present, at the same positions, with similar intensity and width for the studied samples.

Fig. 5 shows the EBSD orientation maps of the cross-section of the produced samples, representing the ZX cross-sections in Fig. 1c, obtained in the center of the samples. The orientation maps and corresponding inverse pole figures reveal a strong <101> texture for all samples. The microstructure consists of large elongated grains that are aligned along the building direction. However, some of the maps obtained from both the 1 mm and the 3 mm samples did present slightly more random texture, indicating that there are texture variations within a given sample. In addition, the EBSD orientation maps of the cross-sections suggest

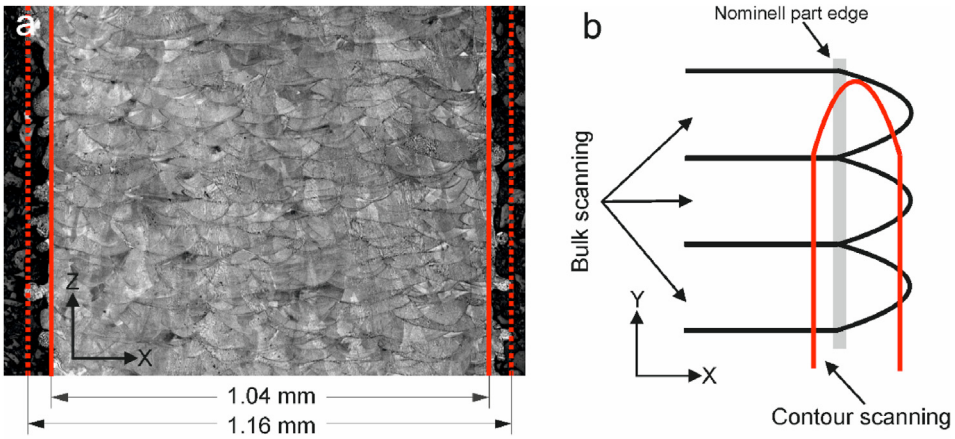

Fig. 2. (a) Light optical image of a ZX cross-section of a 1 mm thick sample. The dashed line represents the thickness, which includes both surface roughness and addition created by the contour scanning. The solid line represents the bulk thickness of the sample. (b) Schematic overview of the contour scanning.

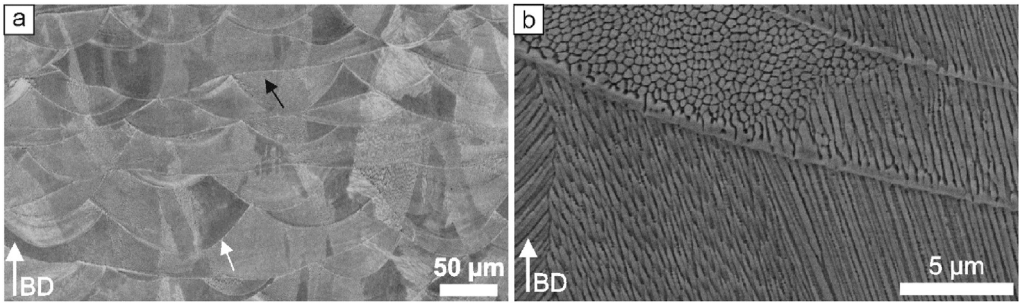

Fig. 3. Cross-section of the standard bar showing (a) low magnification light optical image of the complex microstructure consisting of melt pool boundaries and (b) a high magnification SEM micrograph showing cells with different directions growing across melt pool boundaries. Both cross-sections are obtained along the building direction (ZX).

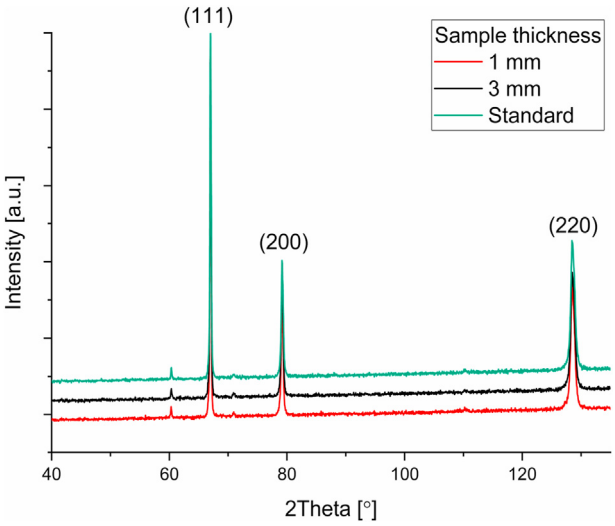

Fig. 4. XRD pattern of as-built 316 L stainless steel samples of standard, 3 mm and 1 mm thicknesses.

that the grain size is not significantly affected by the sample thickness, however an accurate measurement is difficult considering the complex 3D shape of the grains.

High-magnification SEM investigations were conducted on all the as-built samples at various locations. No obvious differences in cell orientation, cell size, or shape were observed when comparing the samples with different thicknesses as well as the standard test bars. Furthermore, no apparent differences in cell orientation, size, or shape were observed when comparing different locations in the samples.

3.2. Mechanical properties

Fig. 6a and b displays representative tensile test curves together with the tensile properties of the L-PBF fabricated samples. The 1 mm thick samples have the lowest yield strength and hence are the weakest among the tested samples. When sample thickness is increased to 3 mm, the yield strength and, consequently, the ultimate tensile strength increases significantly. It can also be observed from Fig. 6 that the 3 mm thick samples achieve a mechanical performance comparable to that of the fabricated standard test samples. It is likewise evident that the elongation to fracture increases with the sample thickness and that the scatter is reduced, as can be seen in Fig. 6b. The thinnest sample exhibits the largest spread in elongation to fracture. This could be a result of the less favorable distribution of defects, such as pores and inclusions. Despite their lower strength, the 1 mm samples still comply with the ASTM A240M-18 standard in terms of minimum yield strength (170 MPa) and ultimate tensile strength (485 MPa) values for 316 L. For all the built samples, the yield strength exceeds the requirement, while still maintaining good ductility. The absence of the usual strength-ductility trade-off for 316 L stainless steel built by L-PBF has been discussed elsewhere (Wang et al., 2018b).

To verify the interpretation of the results, testing of samples with the same dimensions as provided in Fig. 1a was performed on samples that were cut out with a water jet from a 2.5 mm thick 316 L sheet. The tensile test results are presented in Fig. 6c and d. As can be seen, a lower scatter is obtained but with the same trend: 1 mm thick samples presented lower yield strength, ultimate tensile strength values, and elongation to fracture compared to 3 mm thick samples.

The relatively large ductility measured for all the samples is also

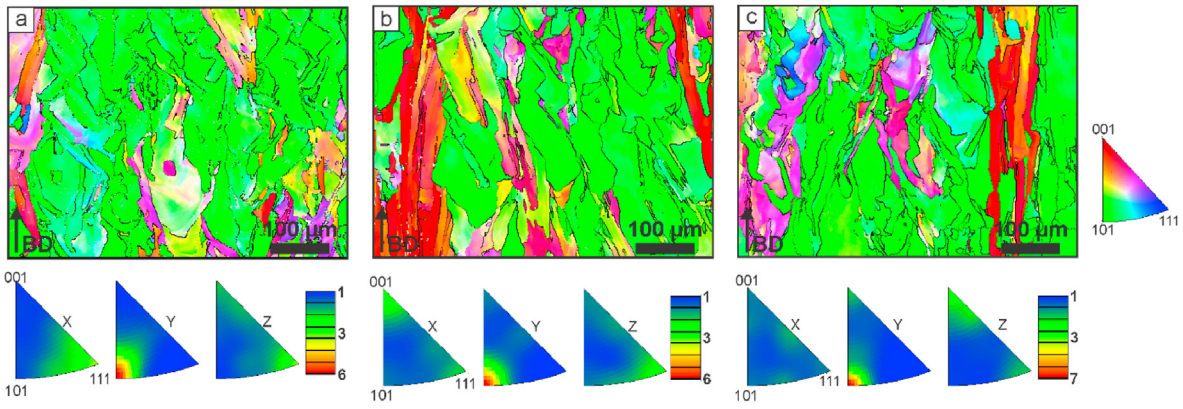

Fig. 5. EBSD orientation maps of cross-section samples (in building direction) from the center of (a) the standard bar, (b) 1 mm thick samples, and (c) 3 mm thick samples. The inverse pole figure color code and the corresponding inverse pole figures are provided.

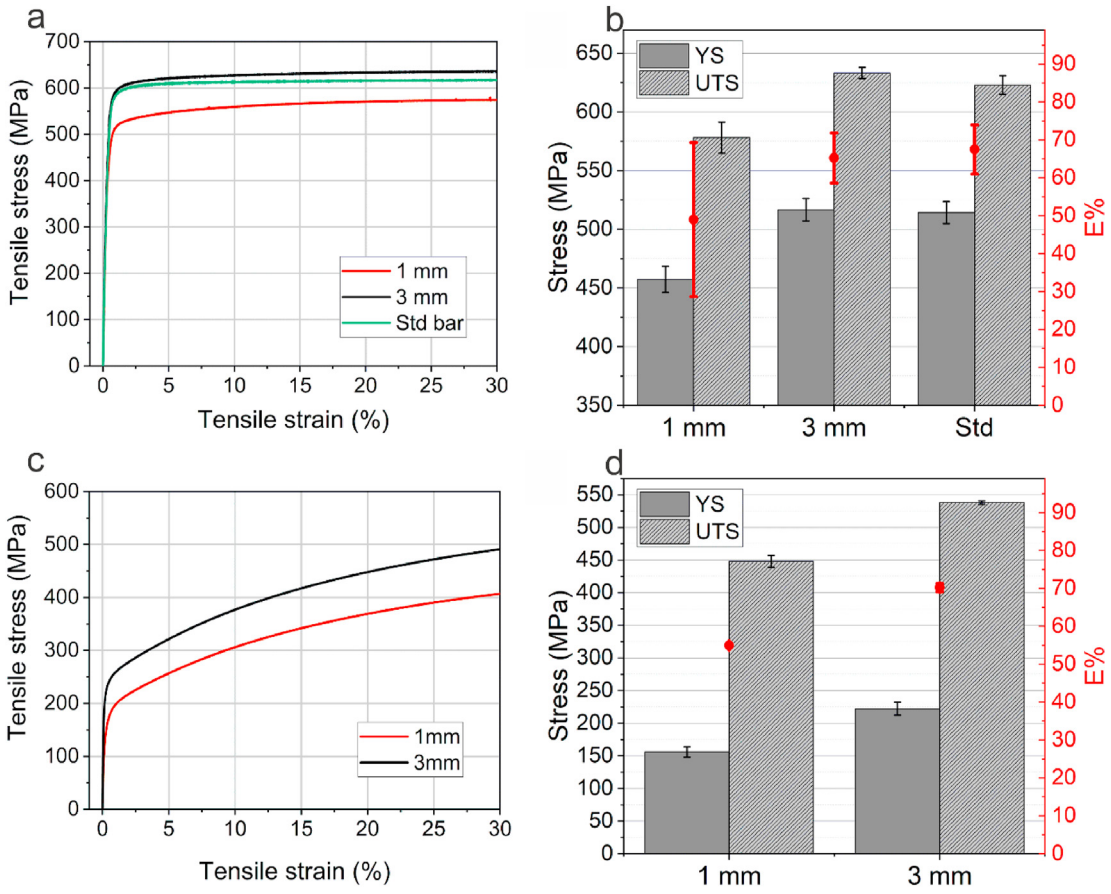

Fig. 6. (a) Engineering stress/strain curves and (b) the average strength and ductility generated from the three different samples produced with L-PBF. (c) Engineering stress/strain curves and (d) the average strength and ductility generated from the three different samples obtained from a metal sheet.

reflected in the appearance of the fracture surfaces; see Fig. 7. Both the 1 mm and the 3 mm specimens are characterized by micron-sized dimples upon failure. Furthermore, evenly distributed spherical oxide inclusions (up to tens of micrometers in diameter) were identified on all fracture surfaces. As shown in Fig. 8, EDX analyses revealed that the oxide particles were rich in Cr, Mn, and Si. As highlighted by Pauzon et al. (2019), they are likely to be thermodynamically stable spinel oxides. The fracture surfaces of samples revealed more cracks and micro-cracks on the 1 mm sample than on the 3 mm sample. This is likely to be attributed to the more significant number of crack initiation points that originate from the surface and are able to propagate and coalesce across the cross-section of the thin specimen. Still, overall, and regardless of the sample thickness, the characteristic failure mechanism observed is transgranular ductile fracture.

4. Discussion

4.1. Microstructure

The preferential growth direction for a face-centered cubic crystal structure is <001>, and several studies have indeed reported strong <001> texture for parts produced with L-PBF (Niendorf et al., 2013; Sun et al., 2018a, 2018b). Many other studies have demonstrated both a strong <101> crystallographic orientation and a more random texture (Wang et al., 2018a; Leicht et al., 2018; Yin et al., 2019; Im et al., 2019). Sun et al. (2019) revealed that the melt pool shape is an essential aspect of texture development in additive manufacturing. It has also been shown that both the size and the shape of the melt pool are strongly affected by the process parameters (Manvatkar et al., 2015; Andreau et al., 2019). Thus, the difference in texture between studies is generated by the

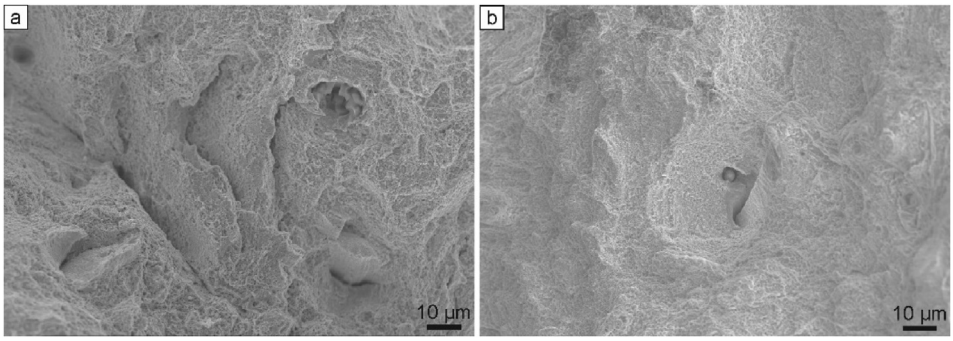

Fig. 7. Micrographs of the fracture surfaces of a (a) 1 mm thick sample, (b) 3 mm thick sample.

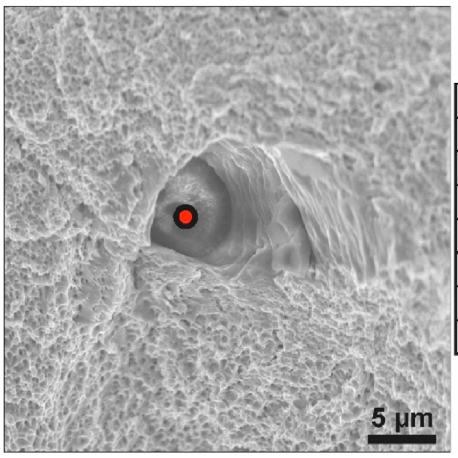

Element	Wt.%
Cr	22.7
Ni	5.8
Mo	1.5
Mn	23.3
Si	0.5
O	5.4
Fe	Bal.

Fig. 8. Spherical oxide inclusion observed on the fracture surface with corresponding chemical composition as obtained by EDX.

different processing parameters, and one cannot take for granted that there is a specific preferential crystallographic orientation during L-PBF. Nevertheless, despite the different processes, Wang et al. (2018a) and Niendorf et al. (2014) showed that when the part thickness is reduced below 1 mm, a stronger <001> texture is created. It would be interesting, therefore, to fabricate the samples provided in this study below 1 mm. However, this was not possible for the applied specimen design since 1 mm was the smallest thickness allowed by the process stability (the build failed below 1 mm because of a too large sample aspect ratio).

4.2. Mechanical properties

The tensile testing demonstrated that both tensile strength and ductility (with lower spread) improved with increased sample thickness. The increased elongation to fracture with increased sample thickness can be expected from pure geometrical considerations since a higher slimness ratio (original length over square root of the cross-sectional area) usually accompanies reduced elongation to fracture (ASM International, 2000). The larger spread in elongation to fracture for the thinnest samples could be a result of the less favorable distribution of defects such as pores and inclusions in connection to the surface-to-volume ratio of the specimen. Even though the volume defect density is small and most probably unchanged, the deformation will be localized earlier when the amount of load-bearing material is reduced. There will still be a higher likelihood for voids to connect, especially considering the connection to surface defects upon deformation. In other words, for thinner samples, voids/-defects will have a shorter distance to the part surface. When a defect grows and eventually reaches a surface defect, failure can occur earlier in the plastic regime.

The surface roughness should not significantly influence the tensile strength even if the samples thickness is reduced (Suh et al., 2010) but it should rather affect the ductility (Scott-Emuakpor et al., 2017). Therefore, the observed reduction in ductility for the 1 mm thick samples might partly be explained by the surface roughness together with the slimness ratio effect. As the total surface area to bulk ratio is increasing when the sample thickness is reduced, the effect of the surface might, therefore, become more significant.

It can be assumed that the nominal thickness of 1 mm represents a condition below a certain critical thickness, while the 3 mm thick sample does not. To depict a specific thickness/grain size ratio for L-PBF is, however, very challenging. The constant movement of the heat source generates grains that are twisted and curved, and the observed grains exhibit a considerable size spread within the same cross-section. This means that the size spread is much larger than the average grain size, as shown in Fig. 5. However, as mentioned, no significant differences in microstructure (cell size, texture, grain orientation, etc.) were observed between the samples with 1 mm and 3 mm nominal thicknesses. Thus, it seems that the size effect is not related to differences in the microstructure.

Therefore, the difference in mechanical properties concerning sample thickness can be explained by the size effect, which is a generic factor. Consequently, when designing AM-fabricated parts, it is essential to consider that mechanical properties of thin sections will deviate from those expected from bulk material properties. It can be expected that there is a critical section thickness below which mechanical properties are less prominent. In the case of bulk samples, a polycrystalline material exhibits a large number of grains that are randomly and evenly distributed. This creates an isotropic deformation behavior. However, when the part thickness is reduced, then fewer grains will take the load, the properties will be differently randomized, and fewer grains will be involved in the overall deformation, such that an inhomogeneous deformation is present (Chan and Fu, 2011). It should be pointed out that the extensive L-PBF literature offers strategies to control the microstructure, and more particularly the grain size, by tuning the laser parameters. It could therefore be of interest to investigate the use of increased laser scanning speed for sample below a critical thickness e.g. 1 mm, to mitigate the size effect. Still, such an adjustment would also have an impact on materials strength, density and defect distribution. It is also worth pointing out that increasing the gauge length (which in this study is relativity large compared to other studies examining size effects) increases the probability of the weakest link.

Furthermore, as the part thickness is reduced, the effect of the surface grains increases (known as surface layer model). The surface grain effect has been explained by, for example, Hug and Keller (2010), who show that the dislocation cells close to the surface are different compared to those inside the part. Grains close to the surface are also less constrained than grains inside the part, which reduces the tensile properties (Hug and Keller, 2010; Miyazaki et al., 1979; Fu and Chan, 2014). As presented by Yang and Lu (2013), the near-surface microstructure, in relation to the internal microstructure, is an essential parameter for the plastic regime. Plastic deformation is always heterogeneous, even for a single-phase material. There will always be locations in a sample that will start to strain before the whole sample does; for example, surface grains do not need to accommodate in the same manner as internal grains, and hence, with increasing surface-to-volume ratio, there is a chance that the yielding will take place more quickly and the overall straining to fracture will be less, as illustrated in this study.

5. Summary and conclusions

The present work highlights the effects of section thickness on the microstructure development and tensile strength of 316 L stainless steel parts produced by L-PBF. The results indicate that fabricating tensile samples with standard dimensions as well as thinner samples using standard process parameters generates a preferential <101> crystallographic orientation along the build direction. The processing resulted in fully dense samples in all cases and mechanical properties that were above the specifications for 316 L stainless steel. Still, the presented tensile test data suggest that reduced part thickness causes a reduction of strength and elongation, even though the measured properties are better than what is required by conventional 316 L. The 3 mm thick samples generated tensile properties comparable to those of standard-dimension samples. The size effect given by specimen thickness in relation to microstructure characteristics like grain size and cell structure is believed to be a governing factor. As a result, there is a reduction in yield strength and consequently lower ultimate tensile strength. Because of the slimness effect, the average elongation to fracture becomes smaller, while the spread increases, possibly related to the distribution of defects. The fracture surfaces for all samples were characterized by micron-sized dimples, with evenly distributed oxides rich in Cr, Mn, and Si. The 1 mm thick samples were characterized with a rougher fracture surface and a higher number of crack nucleation sites compared to the 3 mm sample.

Based on fractography, it was thus assumed that the cracks preferentially initiated from the rough surfaces of the produced parts.

The results emphasize that part thickness must be considered when assessing mechanical response as well as when performing design optimization and simulations, especially for thin-walled structures. In other words, tensile properties from standard tensile test bars might not be useful when estimating properties of thin wall sections and lattice structures.

Declaration of competing interest

The authors declare that they have no known competing financial interests or personal relationships that could have appeared to influence the work reported in this paper.

Acknowledgments

This work has been performed in the framework of the AMLIGHT project within the Innovation programme Metallic Materials and the Center for Additive Manufacturing – Metal (CAM^2), both supported by Swedish Governmental Agency for Innovation Systems (Vinnova).

References

Andreau, O., Koutiri, I., Peyre, P., Penot, J.D., Saintier, N., Pessard, E., De Terris, T., Dupuy, C., Baudin, T., 2019. Texture control of 316L parts by modulation of the melt pool morphology in selective laser melting. J. Mater. Process. Technol. 264, 21–31. https://doi.org/10.1016/j.jmatprotec.2018.08.049.

Asm International, 2000. Handbook committee. ASM Handb. Mech. Test. Eval. 8.

Berman, B., 2012. 3-D printing: the new industrial revolution. Bus. Horiz. 55, 155–162. https://doi.org/10.1016/j.bushor.2011.11.003.

Chan, W.L., Fu, M.W., 2011. Experimental studies and numerical modeling of the specimen and grain size effects on the flow stress of sheet metal in microforming. Mater. Sci. Eng. 528, 7674–7683. https://doi.org/10.1016/j.msea.2011.06.076.

DebRoy, T., Wei, H.L., Zuback, J.S., Mukherjee, T., Elmer, J.W., Milewski, J.O., Beese, A.M., Wilson-Heid, A., De, A., Zhang, W., 2018. Additive manufacturing of metallic components – process, structure and properties. Prog. Mater. Sci. 92, 112–224. https://doi.org/10.1016/j.pmatsci.2017.10.001.

Fu, M.W., Chan, W.L., 2014. Micro-scaled Products Development via Microforming : Deformation Behaviours, Processes, Tooling and its Realization. https://books.google.com/books?id=Yie_BAAAQBAJ&pg=PA100.

Hug, E., Keller, C., 2010. Intrinsic effects due to the reduction of thickness on the mechanical behavior of nickel polycrystals. Metall. Mater. Trans. A Phys. Metall. Mater. Sci. 41, 2498–2506. https://doi.org/10.1007/s11661-010-0286-3.

Im, Y.D., Kim, K.H., Jung, K.H., Lee, Y.K., Song, K.H., 2019. Anisotropic mechanical behavior of additive manufactured AISI 316L steel. Metall. Mater. Trans. A Phys. Metall. Mater. Sci. 50, 2014–2021. https://doi.org/10.1007/s11661-019-05139-7.

Kohyama, A., Hamada, K., Matsui, H., 1991. Specimen size effects on tensile properties of neutron-irradiated steels. J. Nucl. Mater. 179–181, 417–420. https://doi.org/10.1016/0022-3115(91)90113-L.

Kurzynowski, T., Gruber, K., Stopyra, W., Kuźnicka, B., Chlebus, E., 2018. Correlation between process parameters, microstructure and properties of 316 L stainless steel processed by selective laser melting. Mater. Sci. Eng. 718, 64–73. https://doi.org/10.1016/j.msea.2018.01.103.

Leicht, A., Klement, U., Hryha, E., 2018. Effect of build geometry on the microstructural development of 316L parts produced by additive manufacturing. Mater. Char. 143, 137–143. https://doi.org/10.1016/j.matchar.2018.04.040.

Li, H., Ramezani, M., Li, M., Ma, C., Wang, J., 2018. Effect of process parameters on tribological performance of 316L stainless steel parts fabricated by selective laser melting. Manuf. Lett. 16, 36–39. https://doi.org/10.1016/j.mfglet.2018.04.003.

Liverani, E., Toschi, S., Ceschini, L., Fortunato, A., 2017. Effect of selective laser melting (SLM) process parameters on microstructure and mechanical properties of 316L austenitic stainless steel. J. Mater. Process. Technol. 249, 255–263. https://doi.org/10.1016/j.jmatprotec.2017.05.042.

Manvatkar, V., De, A., DebRoy, T., 2015. Spatial variation of melt pool geometry, peak temperature and solidification parameters during laser assisted additive manufacturing process. Mater. Sci. Technol. 31, 924–930. https://doi.org/10.1179/1743284714Y.0000000701.

Miyazaki, S., Shibata, K., Fujita, H., 1979. Effect of specimen thickness on mechanical properties of polycrystalline aggregates with various grain sizes. Acta Metall. 27, 855–862. https://doi.org/10.1016/0001-6160(79)90120-2.

Niendorf, T., Leuders, S., Riemer, A., Richard, H.A., Tröster, T., Schwarze, D., 2013. Highly anisotropic steel processed by selective laser melting. Metall. Mater. Trans. B Process Metall. Mater. Process. Sci. 44, 794–796. https://doi.org/10.1007/s11663-013-9875-z.

Niendorf, T., Brenne, F., Schaper, M., 2014. Lattice structures manufactured by SLM: on the effect of geometrical dimensions on microstructure evolution during processing. Metall. Mater. Trans. B Process Metall. Mater. Process. Sci. 45, 1181–1185. https://doi.org/10.1007/s11663-014-0086-z.

Pauzon, C., Hryha, E., Forêt, P., Nyborg, L., 2019. Effect of argon and nitrogen atmospheres on the properties of stainless steel 316 L parts produced by laser-powder bed fusion. Mater. Des. 179, 107873. https://doi.org/10.1016/j.matdes.2019.107873.

Prashanth, K.G., Eckert, J., 2017. Formation of metastable cellular microstructures in selective laser melted alloys. J. Alloys Compd. 707, 27–34. https://doi.org/10.1016/j.jallcom.2016.12.209.

Raulea, L.V., Goijaerts, A.M., Govaert, L.E., Baaijens, F.P.T., 2001. Size effects in the processing of thin metal sheets. J. Mater. Process. Technol. 115, 44–48. https://doi.org/10.1016/S0924-0136(01)00770-1.

Saeidi, K., Gao, X., Zhong, Y., Shen, Z.J., 2015. Hardened austenite steel with columnar sub-grain structure formed by laser melting. Mater. Sci. Eng. 625, 221–229. https://doi.org/10.1016/j.msea.2014.12.018.

Sames, W.J., List, F.A., Pannala, S., Dehoff, R.R., Babu, S.S., 2016. The metallurgy and processing science of metal additive manufacturing. Int. Mater. Rev. 6608, 1–46. https://doi.org/10.1080/09506608.2015.1116649.

Scott-Emuakpor, O., George, T., Henry, E., Holycross, C., Brown, J., 2017. As-built geometry and surface finish effects on fatigue and tensile properties of laser fused titanium 6Al-4V. Proc. ASME Turbo Expo 6, 1–11. https://doi.org/10.1115/GT2017-63482.

Senthilkumaran, K., Pandey, P.M., Rao, P.V.M., 2009. Influence of building strategies on the accuracy of parts in selective laser sintering. Mater. Des. 30, 2946–2954. https://doi.org/10.1016/j.matdes.2009.01.009.

Strnadel, B., Brumek, J., 2013. Effect of tensile test specimen size on ductility of R7T steel. Met 560–565, 2013 - 22nd Int. Conf. Metall. Mater. Conf. Proc.

Suh, C.H., Jung, Y.C., Kim, Y.S., 2010. Effects of thickness and surface roughness on mechanical properties of aluminum sheets. J. Mech. Sci. Technol. 24, 2091–2098. https://doi.org/10.1007/s12206-010-0707-7.

Sun, Z., Tan, X., Tor, S.B., Chua, C.K., 2018a. Simultaneously enhanced strength and ductility for 3D-printed stainless steel 316L by selective laser melting. NPG Asia Mater. 10, 127–136. https://doi.org/10.1038/s41427-018-0018-5.

Sun, S.H., Hagihara, K., Nakano, T., 2018b. Effect of scanning strategy on texture formation in Ni-25 at.%Mo alloys fabricated by selective laser melting. Mater. Des. 140, 307–316. https://doi.org/10.1016/j.matdes.2017.11.060.

Sun, S.-H., Ishimoto, T., Hagihara, K., Tsutsumi, Y., Hanawa, T., Nakano, T., 2019. Excellent mechanical and corrosion properties of austenitic stainless steel with a unique crystallographic lamellar microstructure via selective laser melting. Scripta Mater. 159, 89–93. https://doi.org/10.1016/j.scriptamat.2018.09.017.

Thomas, D., 2016. Costs, benefits, and adoption of additive manufacturing: a supply chain perspective. Int. J. Adv. Manuf. Technol. 85, 1857–1876. https://doi.org/10.1007/s00170-015-7973-6.

Wang, D., Song, C., Yang, Y., Bai, Y., 2016. Investigation of crystal growth mechanism during selective laser melting and mechanical property characterization of 316L stainless steel parts. Mater. Des. 100, 291–299. https://doi.org/10.1016/j.matdes.2016.03.111.

Wang, X., Muñiz-Lerma, J.A., Sánchez-Mata, O., Attarian Shandiz, M., Brochu, M., 2018a. Microstructure and mechanical properties of stainless steel 316L vertical struts manufactured by laser powder bed fusion process. Mater. Sci. Eng. 736, 27–40. https://doi.org/10.1016/j.msea.2018.08.069.

Wang, Y.M., Voisin, T., Mckeown, J.T., Ye, J., Calta, N.P., Li, Z., Zeng, Z., Zhang, Y., Chen, W., Roehling, T.T., Ott, R.T., Santala, M.K., Depond, P.J., Matthews, M.J., Hamza, A.V., Zhu, T., 2018b. Additively manufactured hierarchical stainless steels with high strength nd ductility. Nat. Mater. 17 https://doi.org/10.1038/NMAT5021.

Yang, L., Lu, L., 2013. The influence of sample thickness on the tensile properties of pure Cu with different grain sizes. Scripta Mater. 69, 242–245. https://doi.org/10.1016/j.scriptamat.2013.04.009.

Yin, Y.J., Sun, J.Q., Guo, J., Kan, X.F., Yang, D.C., 2019. Mechanism of high yield strength and yield ratio of 316 L stainless steel by additive manufacturing. Mater. Sci. Eng. 744, 773–777. https://doi.org/10.1016/j.msea.2018.12.092.

Zhong, Y., Liu, L., Wikman, S., Cui, D., Shen, Z., 2016. Intragranular cellular segregation network structure strengthening 316L stainless steel prepared by selective laser melting. J. Nucl. Mater. 470, 170–178. https://doi.org/10.1016/j.jnucmat.2015.12.034.